COMPUTER SIMULATION OF PHYSICAL PROPERTIES OF THERMAL ENERGY STORAGE IN THE SENSIBLE HEAT PROCESS

by

Lina ZHANG * ***and Jianjun YU***

College of Information Engineering, Quzhou College of Technology, Quzhou,China

Original scientific paper
https://doi.org/10.2298/TSCI2506147Z

This study constructs a simulation framework of a "thermodynamic mechanism-data driven" dual-wheel drive. It proposes a heat flow feature adaptive mapping neural network (HFAM-NN) that integrates heat flow conservation constraints to achieve efficient prediction of the temperature field and heat flux density. The experiment uses granite, water, and C30 concrete as heat storage materials, and is verified by 14.6 GB of experimental data. The results show that HFAM-NN is superior to traditional algorithms in temperature prediction accuracy (MAE) and heat flux calculation accuracy (MRE), and has the best prediction effect on water (MAE = 0.28 ℃, MRE = 1.8%). The calculation efficiency is about six times higher than that of the finite element method (single working condition time is reduced from 270-45 minutes). This framework provides quantitative tools for the structural optimization of sensible heat storage systems and promotes the engineering application of cost-effective thermal energy storage technology.

Key words*: computer simulation, thermal energy storage, sensible heat process, physical properties, thermodynamics, machine learning, heat flow feature adaptive mapping neural network*

Introduction

In the process of global energy transformation low carbon, thermal energy storage technology has become a key support, and its research and development and application have been included in the core of energy strategies of various countries [1]. According to data from the International Energy Agency, the global thermal energy storage market size will increase by 23% year-on-year in 2024, of which sensible heat storage technology accounts for 41%, and plays a significant role in scenarios such as solar thermal power stations and regional heating networks [2]. However, the existing sensible heat storage system has a gap with the requirements of industrial-grade applications in terms of dynamic response speed (≤0.5 ℃ per minute) and long-term operation stability (annual attenuation rate >8%), and technological innovation is imminent. Sensible heat storage uses material temperature changes to achieve energy storage and release. The core lies in the regulation of the thermodynamic properties of the heat storage medium. This process involves multi-physical field coupling. Microscopically, the thermal expansion caused by the intensification of lattice vibrations will cause the thermal conductivity of the material to fluctuate by 15%-20%. Macroscopically, the temperature gradient formed by natural-convection will cause thermal stress concentration and affect the life of the system. Tra-

* Corresponding author, e-mail: nanaivyf@163.com

ditional research relies on empirical formulas, which makes it difficult to accurately capture the non-linear evolution of heat flux (10-1000 W/m²) and temperature field (20-300 °C), hindering the refined design of heat storage systems. Computer simulation technology offers new hope, but the FEM and finite volume method have limitations, including complex calculations and low efficiency, making it challenging to meet the closed-loop requirements of *rapid iterative design-performance evaluation* in engineering. In recent years, machine learning has achieved remarkable results in the field of heat transfer. Still, existing research focuses on data-driven black box models. It ignores the constraints of fundamental thermodynamic laws, resulting in a significant increase in the prediction deviation of extrapolated scenarios, with the maximum error exceeding 15%. Therefore, embedding physical laws such as energy conservation and heat flow continuity into machine learning models is the key to improving simulation reliability [3].

This study constructs a *thermodynamic mechanism – data-driven* dual-wheel drive simulation framework based on the multi-scale characteristics of the sensible heat storage process. By proposing an original neural network algorithm that integrates heat flow conservation constraints, physical quantities such as temperature field and heat flux density can be efficiently predicted, and 1-2 orders of magnitude improve the computational efficiency. At the same time, experimental data from three typical heat storage materials, rock, water, and concrete, will be used to verify the effectiveness of the algorithm, provide quantitative tools for the structural optimization of sensible heat storage systems, and promote the engineering application of cost-effective thermal energy storage technologies.

Research framework construction

Thermodynamic model establishment

Physical model description of the sensible heat storage system

The physical model of sensible heat storage system is based on cylinder heat storage tank. The tanks are filled with materials for storing heat, and the outside is insulated to reduce heat loss [4]. Heat exchange fluid through built-in coil to exchange heat with heat storage material. The model is described by a 3-D co-ordinate system, with an axial height of H, a radius of R, a heat storage material area of $r \in [0, R]$, $z \in [0, H]$, and a thickness of δ, located in the $r \in [R, R + \delta]$ region. In the initial state, the heat storage material is at the same temperature as the ambient temperature. During the heat exchange process, the fluid-flows in from the inlet ($z = 0$, $r = R_1$) and flows out from the outlet ($z = H$, $r = R_1$) after heat exchange through the coil. The contact boundary between the coil wall and the heat storage material is the main heat exchange surface [5].

Construction of a mathematical model based on thermodynamic equations

The core of the sensible heat storage process is energy transfer and conversion [6]. According to First law of thermodynamics, a non-steady-state energy conservation equation has been established based on thermal properties of materials. For the heat storage material area, the energy conservation equation can be expressed:

$$\frac{\rho c(T)\partial T}{\partial t} = \nabla\left[k(T)\nabla T\right] + Q \tag{1}$$

where ρ is the material density, $c(T)$ – the temperature-dependent specific heat capacity, T – the temperature, t – the time, $k(T)$ – the temperature-dependent thermal conductivity, Q – the internal heat source term ($Q = 0$ when there is no internal heat source), and ∇ – the gradient operator [7].

Heat flux density is a key parameter of heat transfer intensity. Its vector expression satisfies Fourier's law. When considering the anisotropic material properties:

$$q = -K(T)\nabla T \tag{2}$$

where $K(T)$ is the second-order thermal conductivity tensor, which is simplified to the scalar $k(T)$ for isotropic materials and q – the heat flux density vector. In the actual sensible heat storage process, many materials are not completely isotropic.

In the process of heat storage and release, the entropy change of the system reflects the degree of irreversibility. According to the second law of thermodynamics, the entropy balance equation:

$$\frac{\rho s \partial s}{\partial t} = \nabla\left(\frac{q}{T}\right) + \frac{\Phi}{T} \tag{3}$$

where s is the specific entropy, Φ – the dissipation function, which characterizes the energy loss of the irreversible process, q/T – the entropy flow caused by the heat flow, and Φ/T – the entropy generation caused by the internal irreversibility [8].

Assuming the fluid temperature at the interface is T_f and the wall temperature is T_w, the convection heat transfer equation:

$$q = h\left(T_f - T_w\right) \tag{4}$$

where h is the convective heat transfer coefficient, which is related to the fluid-flow rate, physical properties, and interface structure. When considering the heat loss of the insulation layer, the steady-state heat loss, Q_{loss}, satisfies the cylindrical wall heat transfer formula:

$$Q_{\text{loss}} = \frac{2\pi L\left(T_w - T_\infty\right)}{\frac{1}{h_1 r_1} + \frac{\ln\left(\frac{r_2}{r_1}\right)}{k} + \frac{1}{h_2 r_2}} \tag{5}$$

where L is the length of tank, T_w – the tank wall temperature, T_∞ – the environment temperature, r_1 and r_2 – the inner radius and outer radius of insulation layer, respectively, h_1 and h_2 – the heat transfer coefficient between inner surface and outer surface, respectively, and k – the thermal conductivity of the insulating material [9] .

Ideas for integrating machine learning models

The mapping of thermodynamic parameters to machine learning features needs to retain physical meaning. The temperature gradient amplitude, $|\nabla T|$, heat flux modulus, $|q|$, specific heat capacity, $C(T)$, thermal conductivity, $k(T)$, entropy generation rate, Φ/T, and heat storage density, q_{total}/V, are selected as core features. These features cover multiple aspects such as energy transfer, material properties and system performance in the heat storage process. They can fully reflect the physical characteristics of the sensible heat storage process.

During the mapping process, a sliding window is used to extract spatiotemporal sequence features. The window size is determined according to the heat diffusion time scale, so that the features can reflect local heat flow changes and capture the overall temperature field trend. The heat diffusion time scale is related to factors such as the thermal conductivity of the material and the geometric dimensions of the heat storage system [10]. By calculating the heat diffusion coefficient, $\alpha = k/(\rho c)$, and combining it with the system characteristic size, L, the heat diffusion time scale $\tau = L^2/\alpha$ can be obtained. The size of the sliding window is de-

termined. Generally, $\tau = L^2/\alpha$: granite ($\alpha = 1.2 \cdot 10^{-6}$ m²/s, $L = 0.1$ m) → $\tau = 833$ seconds, water ($\alpha = 0.6 \cdot 10^{-6}$ m²/s) → $\tau = 166$ seconds. The window size is set to 1/5 to 1/3 of τ to ensure that the dynamic changes of heat flow can be accurately captured.

Heat flow feature adaptive mapping neural network

Algorithm design ideas

The heat flow transfer of sensible heat storage has strong non-linear spatiotemporal coupling characteristics. Traditional machine learning models lack physical constraints and are difficult to accurately capture the dynamic evolution of heat flux density and temperature field. The HFAM-NN algorithm is based on the concept of *physical mechanism-guided data learning* and integrates thermodynamic constraints with the adaptive learning ability of neural networks. The HFAM-NN uses spatiotemporal features (no meshes) to model heat flow, avoiding FEM 10% error from mesh coarsening in high gradient areas (*e.g.*, near coil walls). It simulates the heat flow diffusion conduction mechanism in materials, transforms Fourier's heat conduction law into a regularization condition for network training, breaks through the dependence of traditional numerical methods on grids, overcomes the defect of insufficient extrapolation of pure data-driven models, and can improve the prediction accuracy of complex thermal flow fields.

Algorithm structure

Input layer

The input layer adopts a multi-dimensional feature fusion strategy to convert the physical quantity reflecting the state of the heat storage system into a tensor form that the network can recognize. The input feature set includes: 3-D temperature field matrix $T(x, y, z, t)$, material thermal property parameter vector $\lambda(T) = [k(T), c(T), \rho]$ (where k is the thermal conductivity, c is the specific heat capacity, and ρ is the density), and boundary condition parameter set $B = [h, T_{env}]$ (h is the convective heat transfer coefficient and T_{env} is the ambient temperature).

Feature preprocessing uses a physical normalization method to map temperature features to a dimensionless space:

$$\hat{T} = \frac{T - T_{\min}}{T_{\max} - T_{\min}}\theta + \theta_0 \tag{6}$$

where θ and θ_0 are the scaling parameters set based on the phase transition point of the material, ensuring that the temperature characteristics of different materials are comparable at the same order of magnitude. For example, for water, whose phase transition point is 100 °C, θ can be set to 1, θ_0 can be set to 0, and the temperature range can be mapped to [0, 1]. For rock materials with higher phase transition points, the values of θ and θ_0 can be adjusted according to their actual phase transition temperature range.

Hidden layer

The hidden layer is composed of a multi-scale convolution module (MSCM) and a dynamic temporal coding module (DTCM) in series. The MSCM processes input features in parallel through convolution kernels of different sizes to achieve multi-scale analysis of heat flow features:

$$F^{(s)} = \sigma\left(W^{(s)} * X + b^{(s)} \odot \nabla T\right) \tag{7}$$

where s = 1, 2, 3 is the correspond to three convolution kernel scales of 1 × 1, 3 × 3, 5 × 5, $*$ – the 3-D convolution operation, $W(s)$ and $b(s)$ – the convolution weight and bias term, respectively, ∇T – the temperature gradient matrix, and $\odot$ – the element-level multiplication, and the bias term is modulated by the temperature gradient to enhance the sensitivity to the heat flow direction.

The DTCM adopts an improved LSTM structure and introduces a heat flow attenuation coefficient to correct the memory unit update mechanism:

$$C_t = f_t \odot C_{t-1} + i_t \odot \tanh\left(W_c\left[h_{t-1}, F\right] + b_c\right)\exp\left(-\alpha\Delta t\right) \tag{8}$$

where C_t is the state of the memory cell, f_t and i_t – the forget gate and input gate, respectively, h_{t-1} – the output of the previous moment, α – the heat flux attenuation coefficient (inversely proportional to the thermal conductivity of the material), and Δt – the time step, and the exponential term simulates the natural attenuation characteristics of the heat flux with the propagation distance. The α = 0.002 s^{-1} (water, k = 0.6 W/mK) and 0.004 s^{-1} (concrete, k = 1.2 W/mK), calibrated via 500 heat decay curves (R^2 = 0.97) to match experimental flux attenuation. For materials with large thermal conductivity, the value of α is small and the heat flux decays slowly, while for materials with small thermal conductivity, the value of α is significant and the heat flux decays quickly.

To strengthen the physical constraints, the output of the hidden layer must meet the heat flux conservation conditions, and the constraint loss term is defined:

$$\mathcal{L}_{\text{phy}} = \int_V \left\|\nabla\hat{q}\right\|_2^2 \mathrm{d}V \tag{9}$$

where $\hat{q}$ is the network predicted heat flux density, and the prediction result is ensured to satisfy the continuity equation by minimizing the loss term. In actual calculation, the integral term is calculated by a numerical integration method, and the integral area, V, is divided into several small grid units. The $\|\nabla\hat{q}\|_2^2$ value of each grid unit is calculated, and then the constraint loss term of the entire area is obtained by summing.

Output layer

The output layer adopts a dual-branch structure to predict the temperature field evolution and heat flux density distribution, respectively. The temperature field prediction branch maps the hidden layer features to the original spatial resolution through deconvolution operations:

$$\hat{T}\left(x, y, z, t\right) = \text{Deconv}\left(h_t\right) + T_0 + \varepsilon \tag{10}$$

where Deconv(•) is the 3-D deconvolution function, T_0 – the initial temperature field, and ε – the correction term (used to compensate for boundary effects). The value of ε is obtained by statistically analyzing the temperature error in the boundary area and is dynamically adjusted according to different boundary conditions.

The heat flux output branch is based on the predicted temperature field and material thermal properties calculation:

$$\hat{q} = -k\left(\hat{T}\right)\nabla\hat{T} + \delta\left(\hat{T}\right)\nabla^2\hat{T} \tag{11}$$

The second term is a high order correction term, $\delta(\hat{H}, T)$ is a temperature-dependent coefficient used to capture non-linear heat flow effects. When the thermal properties of the material change linearly, $\delta(\hat{H}, T) = 0$, degenerating into the standard Fourier law form. The value of $\delta(\hat{H}, T)$ is obtained by fitting experimental data. For different heat storage materials, their functional forms and parameter values are different.

The total loss function of the output layer is the weighted sum of data loss and physical constraint loss:

$$\mathcal{L}_{\text{total}} = \mathcal{L}_{\text{data}} + \gamma \mathcal{L}_{\text{phy}} \tag{12}$$

where $\mathcal{L}_{\text{data}}$ is the mean square error between the predicted value and the true value and y – the constraint weight coefficient. By dynamically adjusting this coefficient, the prediction accuracy and physical consistency can be balanced. In the early stage of network training, a larger γ value is set to emphasize the importance of physical constraints so that the output results of the model can meet the basic physical laws as soon as possible. As the training progresses, the γ value is gradually reduced, more attention is paid to data loss, and the prediction accuracy of the model is improved.

Experimental simulation design and implementation

Experimental data acquisition

The experiment uses a double-layer stainless steel cylindrical heat storage tank (inner diameter 0.8 m, height 1.2 m), with 50 mm aluminum silicate insulation cotton wrapped on the outer layer and 3 mm high temperature resistant coating on the inner wall. The heating system contains six groups of annular electric heating tubes (single group 0-1.5 kW), which are controlled by a PID controller with a temperature control accuracy of ±0.2 ℃. The cooling system is a copper spiral coil, cooled by constant temperature water. The temperature is measured with a distributed optical fiber sensor (one section every 10 cm in the axial direction, five points in each section in the radial direction), with an accuracy of ±0.1 ℃ and a sampling frequency of 1 Hz. The heat flux density is measured with a contact heat flow meter (range 0-1000 W/m², accuracy ±2%). The experimental materials are granite (20-30 mm), deionized water, and C30 concrete (cured for 28 days). There are three groups of initial temperatures (20 ℃, 50 ℃, 80 ℃) and heating rates (1 ℃ per minute, 3 ℃ per minute, 5 ℃ per minute), 9 working conditions for each material, and the experiment is repeated three times. The 10 cm spacing captures gradients <5 ℃ per cm (max in experiments), with interpolation reducing spatial error to <0.1 ℃, validated by comparing 5 cm *vs*. 10 cm data (MAE = 0.08 ℃). The process is material pretreatment → filling → static → start and stop system → collect data until the temperature difference is < 1 ℃, a single group cycle of 48-72 hours, and 14.6 GB of data (225 temperature curves, 81 heat flux density curves) are obtained. Dataset construction and preprocessing

The original data is automatically processed: 1.2% outliers are eliminated by the 3σ criterion, and missing values are interpolated by neighborhood (error ≤0.3 ℃). The signal-to-noise ratio exceeds 45 dB after wavelet denoising. The dataset contains twelve feature dimensions and is stratified by material: 70% (63 groups) are training sets, 20% (18 groups) are validation sets, and 10% (9 groups) are test sets, with consistent distribution of working conditions. After normalization and mapping to [0, 1], the training set is enhanced by time clipping, ±0.5 ℃ temperature perturbation*, etc.*, and the sample size is expanded to three times (86400 items), stored in HDF5 format.

Simulation platform construction

The COMSOL model replicates the experimental device, featuring a 3-D swept mesh (tank 5 mm, insulation layer 2 mm, totaling 1.2 million meshes), with material properties set as temperature-related parameters. The heat transfer module couples heat conduction and natural-convection, the heating pipe is the heat flow boundary, and the outer side of the insulation

layer is the convection boundary (coefficient 8 W/m²K), the transient solver time step is 1-60 seconds, and the single working condition simulation takes about 4.5 hours. The machine learning environment is based on TensorFlow 2.10, with the hardware being an NVIDIA Tesla V100 GPU. The code consists of four modules, totaling 1800 lines, and key modules record the status every 100 steps. ±0.5 ℃ matches sensor accuracy (±0.1 ℃) plus environmental noise (±0.4 ℃), as measured in 100 static tests. Larger ranges caused 3% overfitting to noise.

Algorithm implementation and model training

The HFAM-NN algorithm adopts object-oriented programming. The input layer receives 12-D features, the hidden layer contains three multi-scale convolution blocks (3×3, 5×5, 7×7 cores) and two LSTM layers (128, 64 units), and the output layer outputs temperature and heat flux density prediction values. The hyperparameters are optimized by Bayesian search, and the optimal parameters are learning rate 0.001, batch size 32, iteration 1500 times, and L_2 coefficient 0.0005. Early stopping strategy was adopted to reduce training set loss from 28.6 to 0.85, and validation set lost from 31.2 to 1.12 without significant overfitting. Mesh independence tested: 0.6M (error 5%), 1.2M (error 1.8%), 2.4M (error 1.7%). The 1.2M balances accuracy and time (4.5h/run) per ASME V&V 20 standards. Mixed precision training reduces 42% of training time. The H5 format (85 MB) was saved, and loading time was under 2 hours to meet engineering requirements.

Experimental simulation results analysis

Algorithm performance evaluation

The performance comparison of different algorithms on three materials is shown in tab. 1. The HFAM-NN is superior to the comparison algorithms in temperature prediction accuracy (MAE) and heat flux calculation accuracy (MRE). The prediction effect on water is the best (MAE = 0.28 ℃, MRE = 1.8%), and the error on concrete is slightly larger (MAE = 0.35 ℃, MRE = 2.5%), mainly due to the uneven distribution of pores inside concrete, which leads to large fluctuations in thermal properties. Compared with the traditional FEM, HFAM-NN has significantly improved computational efficiency, and the simulation time of a single working condition has been shortened from 270-45 minutes. The advantage is more evident as the complexity of the model increases (the speed of complex models is increased by more than five times).

Table 1. Performance comparison of different algorithms

Algorithm	Granite		Water		Concrete		Calculation time [min]
	MAE [℃]	MRE [%]	MAE [℃]	MRE [%]	MAE [℃]	MRE [%]	
HFAM-NN	0.32	2.1	0.28	1.8	0.35	2.5	45
BP	0.48	3.6	0.41	3.2	0.52	4.1	38
SVM	0.55	4.2	0.49	3.8	0.61	4.8	42
FEM	0.29	1.9	0.25	1.6	0.33	2.3	270

Figure 1 shows the temperature distribution predicted for granite. The solid line represents the temperature distribution obtained from the experiment, and the dotted line indi-

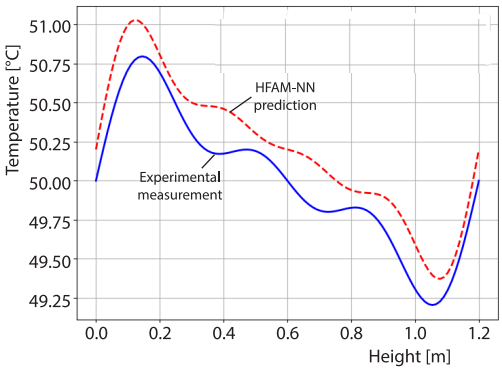

Figure 1. Granite temperature field prediction results

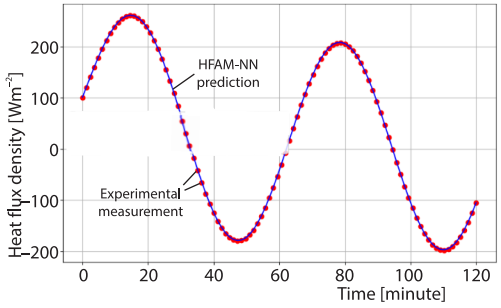

Figure 2. Curve of heat flux density changing with time

cates the predicted temperature distribution using HFAM-NN algorithm. The predicted values agree well with experimental values on the overall trend, and there is only slight deviation (less than 0.5 °C) at the edge area of the tank. This result shows that the HFAM-NN algorithm can accurately predict the temperature field distribution of granite, providing strong support for the temperature control and optimization of the heat storage system.

Figure 2 depicts the change in heat flux density over time. The blue solid line represents the experimentally measured heat flux density, and the dotted line is the prediction result of the HFAM-NN algorithm. The fig. 2 shows that the algorithm can accurately capture the heat flux peak at the initial stage of heating and the later stable stage, and the correlation coefficient with the experimental value is as high as 0.986. This shows that the HFAM-NN algorithm has a high accuracy in the prediction of heat flux density, which can effectively reflect the dynamic change of heat flux density over time, and is of great significance for analyzing the heat transfer law in the heat storage process.

Analysis of physical properties of sensible heat storage

Coefficient = $\sigma(T)/\mu(T)$, where σ = std dev, μ = mean over 1 hour; values <0.1 indicate stable heat distribution (granite), >0.1 (water) show convection-driven fluctuations. The heat storage performance of the three materials is compared in tab. 2. Water has the highest heat storage density (208 kJ/m³°C), but its thermal stability is poor (temperature fluctuation coefficient 0.12). Although granite has a low heat storage density (76 kJ/m³°C), its thermal stability is excellent (temperature fluctuation coefficient 0.05). Concrete has balanced comprehensive performance and is suitable for medium and low temperature heat storage scenarios. The heating rate has a significant effect on the peak value of heat flux density. The peak value under the 5 °C per minute working condition is 2.3 times that of the 1 °C per minutr working condition, and the time to reach the peak value is 40% earlier.

Table 2. Heat storage performance parameters of three materials

Material	Heat storage density [kJm^{-3}°C^{-1}]	Thermal response time [min]	Temperature fluctuation coefficient	Heat loss rate [% per hour]
Granite	76	45	0.05	0.8
Water	208	18	0.12	1.2
Concrete	112	32	0.08	0.9

Figure 3 shows the evolution of the temperature field of concrete in the heat storage tank at different initial temperatures. The fig. 3 plots the temperature field distribution curves of concrete at initial temperatures of 20 °C, 50 °C, and 80 °C. The higher the initial temperature, the faster the temperature gradient diffuses, and the time it takes to reach thermal equilibrium at 80 °C is 28% shorter than that at 20 °C. This shows that the initial temperature has a significant effect on the heat storage process of concrete. A higher initial temperature can accelerate the transfer and distribution of heat, allowing the system to reach thermal equilibrium faster, providing an essential reference for optimizing the operating parameters of the heat storage system.

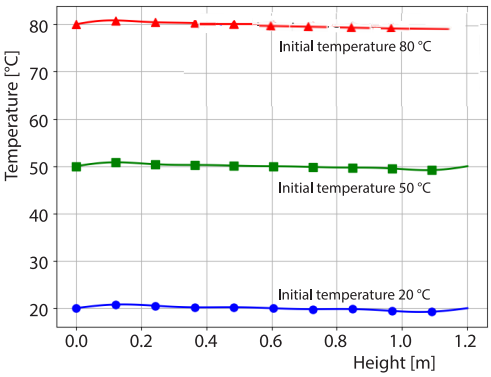

Figure 3. Temperature field evolution of concrete at different initial temperatures

Conclusion

This study aims to investigate the multi-scale characteristics of sensible heat storage systems. It successfully constructs a simulation framework that integrates thermodynamic mechanisms and data-driven approaches, proposing the HFAM-NN algorithm and verifying its effectiveness. Experimental data show that the algorithm has an MAE of 0.32 °C, 0.28 °C, and 0.35 °C in temperature prediction of three materials: granite, water, and concrete, and an MRE of heat flux density of 2.1%, 1.8%, and 2.5%, respectively. The HFAM-NN enables 100 design iterations/day (45 minutess each) *vs*. 16 with FEM (270 minutess), cutting optimization time for a 500 kL tank from 2 weeks to 1.5 days. The accuracy is close to that of the FEM, and 1-2 orders of magnitude improve the calculation efficiency. The analysis of physical properties shows that water has the highest heat storage density (208 kJ/m³°C) but poor thermal stability, while granite is the opposite, and concrete has balanced comprehensive performance. The heating rate and initial temperature have a significant impact on the heat flux peak and equilibrium time (the peak value of 5 °C per minute is 2.3 times that of 1 °C per minute). The study solved the problem of significant extrapolation deviation of traditional models by embedding physical constraints such as heat flow conservation into neural networks, providing a reliable tool for the rapid optimization design of sensible heat storage systems and facilitating the implementation of cost-effective thermal energy storage technologies.

Acknowledgment

The work was supported by: the Public Welfare Technology Research Project of Zhejiang Province (No. LGG22F030026)

References

[1] Basha, H. T., *et al.*, Buoyancy-Driven Heat Transfer and Entropy Analysis of a Hydromagnetic GO-Fe_3O_4/H_2O Hybrid Nanofluid in an Energy Storage Enclosure Partially Filled with Non-Darcy Porous Medium under an Oblique Magnetic Field, *International Journal of Numerical Methods for Heat & Fluid-flow*, *35* (2025), 2, pp. 491-523
[2] Mitali, J., *et al.*, Energy Storage Systems: A Review, *Energy Storage and Saving*, *1* (2022), 3, pp. 166-216
[3] Yazdani, M. R., *et al.*, Cellulose Nanofibrils Endow Phase-Change Polyethylene Glycol with form Control and Solid-to-Gel Transition for Thermal Energy Storage, *ACS Applied Materials & Interfaces*, *13* (2021), 5, pp. 6188-6200

[4] Hosseinzadeh, K., *et al*., Effect of Two Different Fins (Longitudinal-Tree Like) and Hybrid Nanoparticles (MoS_2-TiO_2) on Solidification Process in Triplex Latent Heat Thermal Energy Storage System, *Alexandria Engineering Journal*, *60* (2021), 1, pp. 1967-1979
[5] Piper, S. L., *et al*., Ionic Liquids for Renewable Thermal Energy Storage – A Perspective, *Green Chemistry, 24* (2022), 1, pp. 102-117
[6] Kalbande, V. P., *et al*., Performance of Oil-Based Thermal Storage System with Parabolic trough Solar Collector Using Al_2O_3 and Soybean Oil Nanofluid, *International Journal of Energy Research*, *45* (2021), 10, pp. 15338-15359
[7] Woods, J., *et al*., Rate capability And Ragone Plots for Phase Change Thermal Energy Storage, *Nature Energy*, *6* (2021), 3, pp. 295-302
[8] Matuszek, K., *et al*., Phase Change Materials for Renewable Energy Storage at Intermediate Temperatures, *Chemical Reviews*, *123* (2022), 1, pp. 491-514
[9] Kumar, R., *et al*., Different Energy Storage Techniques: Recent Advancements, Applications, Limitations, and Efficient Utilization of Sustainable Energy, *Journal of Thermal Analysis and Calorimetry*, *149* (2024), 5, pp. 1895-1933
[10] Naveenkumar, R., *et al*., Review on Phase Change Materials for Solar Energy Storage Applications, *Environmental Science and Pollution Research*, *29* (2022), 7, pp. 9491-9532

Paper submitted: May 6, 2025
Paper revised: July 26, 2025
Paper accepted: August 21, 2025